IEEE Access
Multidisciplinary | Rapid Review | Open Access Journal

Received July 11, 2020, accepted July 20, 2020, date of publication July 27, 2020, date of current version August 5, 2020.

Digital Object Identifier 10.1109/ACCESS.2020.3012029

Step-Down Switched-Inductor Hybrid DC-DC Converter for Small Power Wind Energy Conversion Systems With Hybrid Storage

OCTAVIAN CORNEA[1], (Member, IEEE), DAN HULEA[1], (Student Member, IEEE), NICOLAE MUNTEAN[1], (Senior Member, IEEE), AND GHEORGHE-DANIEL ANDREESCU[2], (Senior Member, IEEE)

[1]Electrical Engineering Department, Politehnica University Timisoara, 300006 Timisoara, Romania
[2]Department of Automation and Applied Informatics, Politehnica University Timisoara, 300006 Timisoara, Romania

Corresponding author: Octavian Cornea (o.cornea.upt@gmail.com)

This work was supported by the Romanian Ministry of Research and Innovation, PERFORM-TECH-UPT—"The increasing of the institutional performance of the Politehnica University Timisoara by strengthening the research, development and technological transfer capacity" in the field of "Energy, Environment and Climate Change" under Grant 10PFE/16.10.2018.

ABSTRACT This work is focused on a step-down switched-inductor hybrid dc-dc converter (SIHDC) integrated in a small power wind energy conversion system (WECS). The converter has two roles, to maintain the wind turbine at the maximum power point by controlling the electric generator loading, and to charge a high power density supercapacitor, which is part of a hybrid storage unit that also contains rechargeable batteries. The paper points out the steady-state analysis of the converter in continuous and discontinuous current modes, specific for this application. The stability investigation is presented in detail, including the influence of the electrical generator. The parameterized small-signal transfer function of the control variable derived in this paper can be used to quickly obtain the information needed to evaluate the stability of any similar WECS. A current controller was designed to achieve a stable operation in continuous current mode, and afterwards the stability was checked for discontinuous current mode. A 5kW step-down SIHDC prototype was built and extensively tested, both in laboratory, by using a wind turbine emulator, and in a small power (5kW) WECS industrial platform. Experimental results obtained under real operating conditions confirm the theoretical analysis and laboratory tests, showing that SIHDC converter is a valid solution for low power wind energy conversion systems.

INDEX TERMS Hybrid dc-dc converters, renewable energy, stability analysis, step-down dc-dc converters, switched-inductor, wind energy conversion system, wind turbine.

I. INTRODUCTION

The main goal of a wind energy conversion system (WECS) is to get the maximum available power from the wind turbine at each moment. This is done by loading the electrical generator in accordance with the wind speed, in order to keep the operation at the maximum power point of the wind turbine power-speed characteristic.

For medium and high-power wind energy applications, back-to-back three-phase converter topologies are used to transfer the power from the wind turbine to the grid, while at the same time providing reactive and active power control [1]–[3].

On the other hand, for low power turbines, up to 10kW, the use of three-phase controlled rectifiers is generally considered too expensive. In these cases, the three-phase output voltage of the electric generator is rectified by a diode bridge and a DC-DC converter is used to set the generator output power. A classical boost converter is suitable for this application [4]–[7] if the converter output voltage bus is connected to an inverter, which transfers the power to the local grid.

However, due to the uncontrolled rectification, the electromagnetic torque ripple is relatively large and this fact can have a negative impact on the wind turbine reliability. This issue can be mitigated by a careful control design [5] or by

The associate editor coordinating the review of this manuscript and approving it for publication was Giambattista Gruosso.

replacing the diode bridge with a specially designed "multi-pulse autotransformer rectifier" [7]. A study presented in [6] reveals that for a permanent magnet generator with high number of pole-pairs, the electromagnetic torque ripple is well filtered by the shaft and rotor, so that the mechanical torque ripple amplitude is below 1% of the turbine rated torque.

In small power WECSs with energy storage elements (supercapacitors and/or batteries), the step-down converter topologies are more convenient to use, because the number of storage cells in series in this case can be much lower. Hybrid DC-DC converters [8], [9] are good candidates for this application. By inserting switched-inductor or switched-capacitor cells, passive or active, in standard simple converters (e.g., buck, boost, Cuk, Sepic), new topologies can be obtained, characterized by high or very high voltage conversion ratio for unidirectional [9]–[12], [14] or bidirectional operation [13].

The use of a step-down SIHDC in a WECS was previously reported [15], but an in-depth investigation of the converter integration into the system has not been published in the literature. Nevertheless, this investigation is necessary because the operation can become instable if the stability is not correctly evaluated by taking into consideration the parameters of the electric generator. In addition, in energy conversion systems that contain supercapacitors, as in the case presented in this paper, it must also be taken into account that the converter must operate for a large variation of the output voltage.

Supercapacitors are already present in a range of applications that require high power density: trains and trams propulsion systems, electric vehicles and busses, energy storage systems connected to high power sources, different control functions such as voltage control, frequency regulation and smoothing short term power fluctuations in electric grid, micro- and smart-grids, etc. [16], [17]. Moreover, according to many market forecasts, a high global growth rate is expected in the future years, which can lead to further price reduction and continuous investment in key research projects focused on characteristics improvement.

Due to their high-power density, low maintenance requirements and ability to withstand extreme conditions, the supercapacitors are especially attractive for renewable energy applications [16]. According to recent research, it is possible to obtain supercapacitors with very high power density, while keeping the energy density at a decent value [18], [19]. However, in most applications, currently it is necessary or advantageous to also have rechargeable batteries in the energy storage system. [20], [21]. In this type of hybrid system - similar to the one presented in this paper -, the supercapacitors deal with high power peaks and the batteries are used for storage at high energy density, or as backup devices.

After a review of the switched-inductor hybrid step-down converter theory, the paper presents the following new contributions:

1) An analytical average model of the WECS, including the hybrid converter and a DC equivalent model for the electrical generator;

2) A parameterized small-signal transfer function of the control variable that can be used to quickly assess CCM stability for any similar WECS;

3) A circuit average model which is valid for any similar WECS, operating in CCM or DCM;

4) Current controller design to assure the stability in CCM; stability check in DCM through Bode diagrams;

5) WECS validation through digital simulations and experimental tests conducted in laboratory (using a wind turbine emulator), and in the field, on a 5kW wind turbine industrial platform.

Section II presents the WECS configuration, Section III is for steady-state analysis whereas the stability analysis is presented in Section IV. Simulation and experimental results are described in Section V. The conclusion is drawn in Section VI.

II. WECS CONFIGURATION

The energy conversion system of the small power wind turbine discussed in this paper is presented in Fig. 1. The part of the system located inside the rectangle drawn with dashed line represents the paper scope. The elements situated on the right side of the supercapacitor (SC) have no influence on the system stability and can be modified according with the application requirements. In general, the battery bank is necessary but its capacity can be low, therefore inexpensive (or not expensive) batteries can be used.

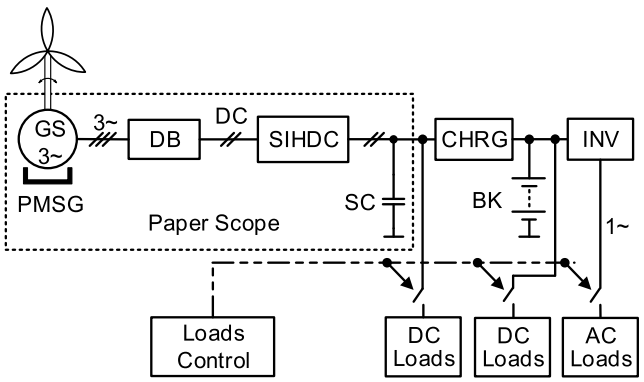

FIGURE 1. Block diagram of a WECS that incorporates a step-down SIHDC which sets the operating point of the electric generator.

A specially designed permanent magnet synchronous generator (PMSG) having a high number of pole-pairs is used to obtain a three phase, variable frequency electrical system with sinusoidal voltages that are rectified by a three-phase diode bridge (DB).

The step-down SIHDC connects DB with the supercapacitor. The hybrid converter has two roles in the energy conversion system:

- It is used to set the operating point of PMSG through the SIHDC input current, which is the controlled variable,

in order to get, at each moment, the maximum power from the generator.
- It charges the supercapacitor, being able to transfer the maximum electrical power from the wind turbine to the converter output.

In normal operation, SC is able to store the energy taken from the wind turbine, even in the case of the maximum available power. It is an energy buffer, connected between PMSG and the battery bank BK that is unable to take high peak power.

The battery bank (four 12V batteries in series) is charged from SC through a DC charger (CHRG), with a maximum current much smaller than SC charging current. An inverter with an internal boost circuit (INV) is used to transform the DC BK voltage in an AC voltage to supply the AC standard loads.

The inverter can also be connected to the AC local grid to inject power in the grid, when the wind energy exceeds local load requirement. CHRG and INV are commercial devices integrated in the system to test the operation in different scenarios.

If the wind speed is high for long time periods, the supercapacitor voltage can increase to the maximum level and the batteries will become fully charged. In order not to waste wind energy, the energy has to be diverted through other components, automatically introduced in circuit by the Loads Control block. It can connect/disconnect two types of DC loads (those fed by the SC voltage and those connected to the battery bank) and AC loads. For very high wind speeds, the system is protected by mechanical means and by completely disconnecting the PMSG from SIHDC input.

The operation of CHRG, INV and Loads Control block is synchronized, so that in all WECS normal operating conditions it is possible to transfer via SIHDC the maximum power which can be obtained from the wind turbine.

The main characteristics and parameters of WECS, including those of SIHDC prototype, are presented in Table 3 and VI-B, Section VI.

III. SIHDC STEADY-STATE ANALYSIS

A. CONTINUOUS CURRENT MODE (CCM)

SIHDC schematic is presented in Fig. 2. For the sake of simplicity, in this section we will discuss the converter operation, considering the input voltage given by a DC source, not by a rectified sinusoidal voltage source. The converter current waveforms and the basic equations are the same in this case as in the case presented in Fig. 1. The influence of PMSG on the energy conversion system, especially on SIHDC operation, is taken into account in section IV, where the stability is investigated.

SIHDC basic theory for steady-state operation was presented in previous papers [8], [9]. This paper focuses on those aspects that are relevant or specific to the WECS application.

Inductors L_1 and L_2 are considered of equal inductance values, in consequence the current waveforms are identical.

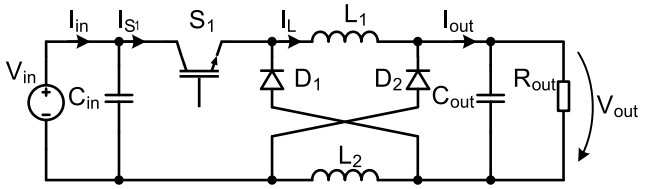

FIGURE 2. Schematic of the step-down SIHDC.

In addition, the analysis requires the power switches S_1, D_1 and D_2 to be ideal.

In CCM operation, the converter can be in one of the two possible states, presented in Fig. 3.

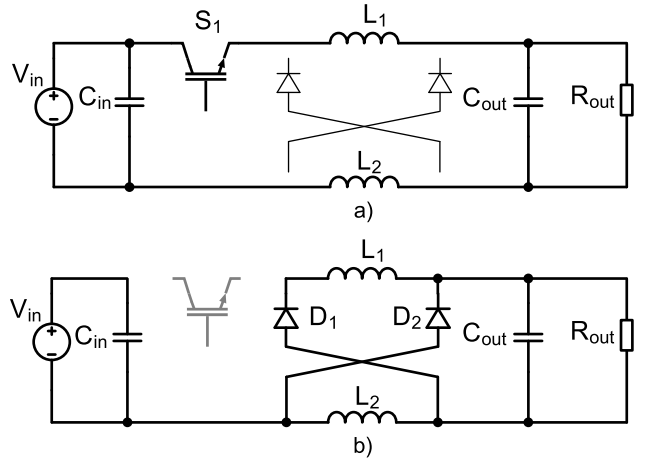

FIGURE 3. SIHDC equivalent circuits: a) for S_1 on; b) for S_1 off.

If S_1 is in conduction, the inductors L_1 and L_2 are connected in series and the energy is accumulated in their magnetic fields. The voltage across one inductor is half of the difference between input and output voltages and is always positive. The current through L_1 is rising linearly, as Fig. 4 shows. In this state, the voltage across the output capacitor is rising, however C_{out} is considered sufficiently large, as the output voltage ripple can be neglected. The current i_{out}, shown in Fig. 2, is equal to the inductor current.

If S_1 is blocked, L_1 and L_2 are connected in parallel through D_1 and D_2. The voltage across one inductor is negative, equal in absolute value to the output voltage. The inductor current is decreasing linearly and a part of the energy from its magnetic field is transferred to the converter output. I_{out} doubles its value at the instant when the diodes switch in conduction mode. Fig. 4 shows that the maximum value of i_{out} is twice the maximum inductor current and its minimum is equal to the minimum inductor current. The AC component of i_{out} waveform is filtered by the output capacitor and the DC component sets the output voltage applied across R_{out}.

If, instead of the resistance R_{out}, energy storage elements are connected at the output, as in Fig. 1, the converter output voltage is set by them, and i_{out} represents the charging current. However, the validity of the facts presented in this section is preserved.

TABLE 1. Comparison of SIHDC with other topologies.

	SIHDC	Buck	H2SC [22]	ID [23]	ID-ID [23]	FOSDC [24]	BBwCC [25] (1 stage)
$M = \frac{V_{out}}{V_{in}}$	$\frac{D}{2-D}$	D	$\frac{D}{(2-D)^2}$	$\frac{2D}{1+D}$	$\left(\frac{2D}{1+D}\right)^2$	$\frac{D^2}{1-D-D^2}$	$\frac{2D}{1-D}$
No. of switches	1	1	1	1	2	1	1
No. of diodes	2	1	5	4	8	3	2
No. of inductors	2	1	3	2	4	2	2
No. of capacitors (including C_{in})	2	2	4	2	3	3	3
Max voltage across S	$V_{in}+V_{out}$ $=\frac{2V_{in}}{2-D}$	V_{in}	$\frac{4-D}{(2-D)^2}\cdot V_{in}$	V_{in}	$V_{S1}=\frac{1+3D}{1+D}V_{in}$ $V_{S2}=V_{in}$	$\frac{V_{in}}{1-D-D^2}$	$\frac{V_{in}}{1-D}$

The voltage conversion ratio, M, characteristic for SIHDC operating in CCM, is obtained by applying the voltage-second balance across one inductor:

$$D \cdot \frac{V_{in} - V_{out}}{2} + (1-D) \cdot (-V_{out}) = 0, \tag{1}$$

$$M = \frac{V_{out}}{V_{in}} = \frac{D}{2-D}, \quad D = \frac{t_{on}}{T}. \tag{2}$$

The duty cycle of S_1 can be expressed by:

$$D = 2 \cdot \frac{V_{out}}{V_{in} + V_{out}} = \frac{2 \cdot M}{1+M}. \tag{3}$$

Equation (2) shows that the output voltage is always lower than input voltage, SIHDC presented in Fig. 2 being a step-down converter.

Due to the term (2-D) at the denominator, its voltage conversion ratio is reduced up to two times in comparison with a classical buck converter, which is an advantage of the hybrid converter.

The following relations between the inductor current i_L, switch current i_{S1} and input current I_{in} are obtained from Fig. 4:

$$i_{L,avg} = \frac{i_{S_1,avg}}{D} = \frac{I_{in}}{D} = \frac{V_{in}+V_{out}}{2 \cdot V_{out}} \cdot I_{in} = \frac{1+M}{2 \cdot M} \cdot I_{in}, \tag{4}$$

$$i_{S_1,\max} = i_{L,\max} = \frac{I_{in}}{D} + \frac{V_{in}-V_{out}}{4L} \cdot T \cdot D. \tag{5}$$

For the wind energy conversion system presented in Fig. 1, I_{in} is the average value of the input current, whose waveform is one specific to a rectified three-phase sinusoidal system.

Equations (4) and (5) allow the estimation of the worst-case values for i_L and i_{S1}, necessary for power switch selection and inductor design.

The voltage stresses of transistor and diodes are given by:

$$V_{S_1} = V_{in} + V_{out} = V_{in} \cdot (1+M), \tag{6}$$

$$V_D = \frac{V_{in}+V_{out}}{2} = \frac{V_{in} \cdot (1+M)}{2}. \tag{7}$$

A comparison between SIHDC and other topologies, including the classic buck converter, regarding the number of active and passive components, the voltage conversion ratio and the transistor maximum voltage stress, is presented in Table 1. Each of these topologies has only one transistor apart from the ID-ID, which contains two. ID, ID-ID and H2SC are hybrid topologies as SIHDC. They incorporate standard switched-capacitor/switched-inductor structures as defined in [8]. FOSDC and BBwCC make use of other passive switching structures.

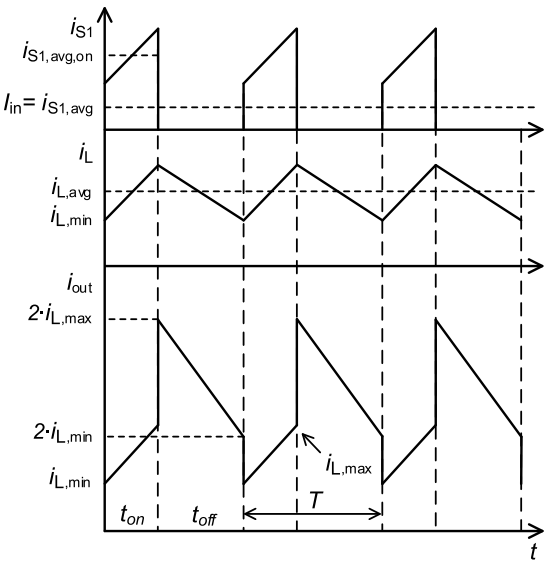

FIGURE 4. SIHDC current waveforms in steady-state CCM operation.

Apart from the other converters from Table 1, BBwCC has also step-up capability. In addition, it allows the stacking of multiple passive switching structures at the output. However, only the one-stage topology is listed in the table because the multiple-stages topologies have worsened characteristics in regard to the application presented in this paper.

In comparison with buck converter, SIHDC has only two additional components, which is the smallest number from all the converters listed in Table 1.

The maximum voltage stress of S_1 switch is always higher for SIHDC than for buck and ID converters. The comparison between SIHDC and the other topologies in this aspect

depends on the operating condition, through D. It can be noted that for SIHDC, as the ratio between the output and input voltages is decreasing, the contribution of V_{out} in the S_1 voltage stress is also decreasing, reducing the maximum value of the voltage across S_1.

Voltage conversion ratios of the converter listed in Table 1 are plotted against D in Fig. 5. A topology with a higher value of D at the given M has better performances for the application presented in this paper. ID and BBwCC converters have lower duty cycles than buck, therefore their use is not convenient for WECS. ID-ID topology presents a duty cycle comparable with that of SIHDC at low M, but it has many additional components, including a second transistor. H2SC converter has a higher D than SIHDC, but it needs six more components. FOSDC topology can be a competitor of SIHDC for low power WECS applications because it has a higher D than SIHDC for $M < 0.3$. However, one diode and one capacitor are additionally needed for FOSDC. Therefore, for step-down applications which do not require a very high decrease in the conversion ratio, the SIHDC is more suitable due to the reduced number of components.

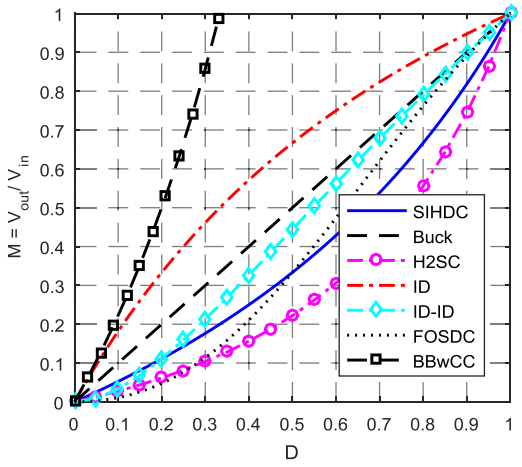

FIGURE 5. Voltage conversion ratios as function of the duty cycle D for the converters listed in Table 1.

Using SIHDC instead of buck converter in the WECS presented in Fig. 1 allows a significant increase in the duty cycle. For $M = 0.1$ and $M = 0.2$, D is higher with 82% and 66% respectively, for the hybrid converter. An increased value of D can have a positive impact on the RMS transistor current, as Table 2 shows. Considering that the two converters operate at the same M, required by the application, the RMS current of SIHDC converter is 26% lower for $M = 0.1$ and 22% lower for $M = 0.2$. This reduction contributes to the efficiency improvement, due to the decreasing of the conduction losses.

On the other hand, the average transistor current is the same for SIHDC and buck converters because it is equal to the average input current, which sets the PMSG and wind turbine operating points.

TABLE 2. RMS, average and peak transistor currents for SIHDC and buck converters.

	Buck	SIHDC
RMS value of S_1 current	$\simeq \sqrt{D} \cdot I_{out}\,[\,\frac{M \cdot I_{out}}{\sqrt{D}}\,]$	$\simeq \frac{\sqrt{D}}{2-D} \cdot I_{out}\,[\,\frac{M \cdot I_{out}}{\sqrt{D}}\,]$
Avg value of S_1 current	$D \cdot I_{out}\,[\,M \cdot I_{out}\,]$	$\frac{D}{2-D} \cdot I_{out}\,[\,M \cdot I_{out}\,]$
Peak value of S_1 current	$\frac{V_{out}}{2 \cdot L \cdot f_s} \cdot (1-D) \quad I_{out}$	$\frac{V_{out}}{2 \cdot L_1 \cdot f_s} \cdot (1-D) + \frac{I_{out}}{2} \quad D$

Regarding the peak value of the transistor current, the reduction is much more pronounced than in the case of the RMS current. The first term in each equation is half of the inductor current ripple which is supposed to be comparable in value for SIHDC and buck converters, being an inductor design input expressed as a percent of the maximum current. Therefore, considering only the second term for comparison, the SIHDC transistor current peak value is reduced with 45% for $M = 0.1$ and with 40% for $M = 0.2$. This significant drop contributes to the efficiency improvement due to the decrease of the transistor current values at switch-on and switch-off moments which results in the switching losses reduction. For lower values than $M = 0.1$, even if the SIHDC converter can be used (it has a duty cycle of 10% at $M = 0.05$), other converters can be more suitable, for example FOSDC.

Even though SIHDC has two extra components, it is a better alternative than buck converter for applications with moderate to high voltage conversion ratio due to the advantages mentioned above.

At the CCM limit, where the inductor current is zero in only one point, the input current has the following form:

$$I_{in,\lim} = D^2 \cdot \frac{V_{in} - V_{out}}{4L} \cdot T = \left(\frac{V_{out}}{V_{in} + V_{out}}\right)^2 \cdot \frac{V_{in} - V_{out}}{L} \cdot T. \tag{8}$$

If the average input current falls below $I_{\text{in,lim}}$, the operation switches to discontinuous current mode.

Using (8) and the prototype data presented in Table 3, Section VI, the 3D surface presented in Fig. 6 was obtained for $I_{\text{in,lim}}$, in V_{in} and V_{out} allowed ranges. There is a large variation of $I_{\text{in,lim}}$, from less than 2A to more than 7A. The highest value corresponds to the operating point with $V_{\text{in}} = 400$V, which means a significant power level is needed at the converter input to assure CCM operation. In addition, $I_{\text{in,lim}}$ does not decrease bellow 6A, if V_{in} is in the range of 200V to 400V, and V_{out} is close to its maximum. Thus, the optimum power point for PMSG can often require an I_{in} below the 3D surface; therefore, the converter has to be able to sustain a stable operation in both continuous and discontinuous current modes.

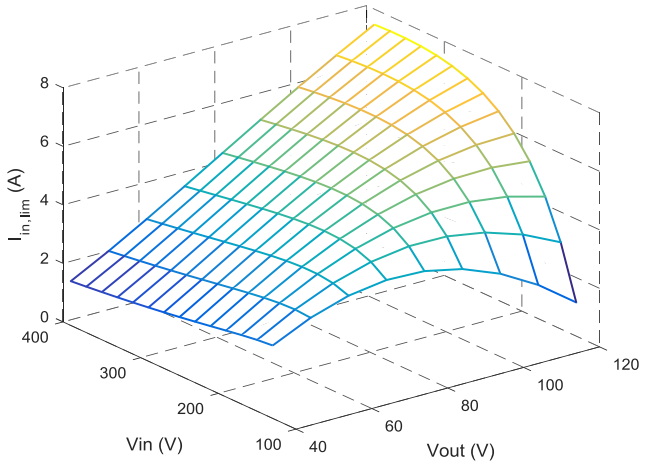

FIGURE 6. Value of I_{in}, at CCM limit, as function of V_{in} and V_{out}.

B. DISCONTINUOUS CURRENT MODE (DCM)

In DCM all the energy accumulated in inductors during t_{on} is transferred to the load when the transistor is off. There is also a time interval with zero inductor current. The waveforms of transistor current, inductor current and output current for a typical situation of DCM are presented in Fig. 7.

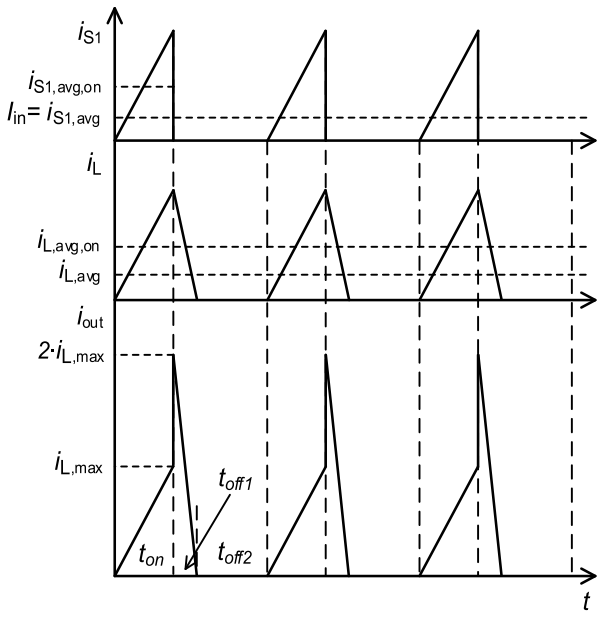

FIGURE 7. SIHDC current waveforms in steady-state DCM operation.

The time interval in which S_1 is off is divided in two parts: in t_{off1} the inductor current is positive, and in t_{off2} it is zero. The inductor current is greater than zero in $t_L = t_{on} + t_{off1}$.

The duty cycle for DCM is given by the equation:

$$D = \frac{t_{on}}{T} = \sqrt{\frac{4 \cdot L \cdot I_{in}}{T \cdot (V_{in} - V_{out})}}. \tag{9}$$

During operation in DCM, the duty cycle is automatically controlled at the value expressed by (9), in which instantaneous input and output voltages are imposed by application, and the average input current is required by the wind turbine maximum power point tracking (MPPT) algorithm.

The voltage conversion ratio for DCM, obtained from (9), is:

$$M_{DCM} = \frac{V_{out}}{V_{in}} = 1 - \frac{4 \cdot L \cdot I_{in}}{D^2 \cdot T \cdot V_{in}} \tag{10}$$

In addition, the following equations can be written:

$$i_{L,avg,on} = \frac{I_{L,\max}}{2} = \frac{i_{S_1,\max}}{2} = \frac{I_{in}}{D}, \tag{11}$$

$$\begin{aligned} t_L &= t_{on} + t_{off1} = \frac{V_{in} + V_{out}}{2 \cdot V_{out}} \cdot D \cdot T \\ &= \frac{1 + M}{2 \cdot M} \cdot D \cdot T, \end{aligned} \tag{12}$$

$$\begin{aligned} i_{L,avg} &= i_{L,avg,on} \cdot \frac{t_L}{T} = \frac{V_{in} + V_{out}}{2 \cdot V_{out}} \cdot I_{in} \\ &= \frac{1 + M}{2 \cdot M} \cdot I_{in}, \end{aligned} \tag{13}$$

$$i_{S_1,\max} = i_{L,\max} = \frac{2 \cdot I_{in}}{D}. \tag{14}$$

The average value of inductor current does not depend on D but on I_{in}, V_{in} and V_{out}. The relation between $i_{L,avg}$ and I_{in} is the same in CCM and DCM.

The transistor and diode stresses are given by the same equations as for CCM.

IV. STABILITY ANALYSIS

In this section, the stability of the electrical subsystem is investigated, in order to obtain the necessary information for current controller design, which guarantees the absence of oscillations in the controlled current.

The WECS system contains two frequency-separated subsystems: the wind turbine (the mechanical subsystem) with a slow time constant, and the electric subsystem with a fast time constant. Therefore, under normal operating conditions, the mechanical subsystem has practically no influence on the electric subsystem.

The converter input current is regulated by a controller with the current reference given by a MPPT method. The controller has to provide stability for any PMSG loading condition.

For the stability analysis two methods were employed to obtain the equivalent average model of the converter: (i) an analytical method, the State Space Averaging Method - SSA, and (ii) a circuit method based on the PWM switch model (PWMSM), which was implemented in a SPICE like simulator.

The SSA method can be applied conveniently for the CCM case. Its application in DCM is not suitable because it is necessary to take into consideration the additional state that appears in DCM, and thus a completely different equivalent average model of the converter is obtained for DCM.

Moreover, a comparison made between SSA and PWMSM methods in the case of a converter stability analysis presented in the literature [28] revealed that the PWMSM method

detected a dynamic phenomenon - whose manifestation was experimentally demonstrated - which did not appear in the frequency characteristic obtained through the SSA method.

In addition, regarding the PWM switch model, the same equivalent average model can be used for CCM and DCM. It can be used even if the reference value of the controlled variable changes in the simulation model in a way that determines the transition from one mode to the other. Considering these aspects, PWMSM method could have advantages over SSA method. However, it needs to be checked against SSA, due to the reason explained in section IV B.

On the other hand, the SSA method has the advantage that it can be used to obtain a parameterized (analytical) small-signal transfer function of the control variable for CCM, which can be quickly customized for any similar WECS, and then employed for stability assessment and current controller design.

A. STATE SPACE AVERAGING (SSA) METHOD

SSA is a classical analytical method used for stability analysis [27] for switching power converters. It is based on a continuous-time, average mathematical model of the converter, in which all the operating states of a switching period contribute in a weighted way, depending on the time interval for each state.

In this section, SSA method is used to determine the equivalent average model for steady-state converter operation in CCM. This model is then employed for stability assessment.

To apply this method for the system presented in Fig. 1, however, it is not sufficient to consider only the circuit model of the converter, as it is usually done. The circuit model of PMSG has to be taken into account also, because inductances of the three phases have a relevant impact on the stability.

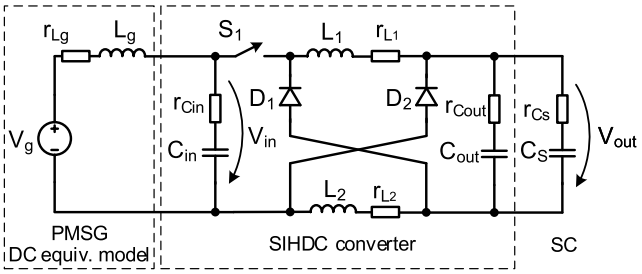

FIGURE 8. Schematic for stability analysis, that contains the SIHDC converter with parasitic elements and a DC equivalent model of PMSG.

The schematic shown in Fig. 8 is adapted to obtain the small-signal transfer functions, which determines the system stability. The assembly comprising the electric generator and the diode bridge from Fig. 1, used to supply the converter, was replaced by a DC equivalent model, containing the voltage source V_g, the equivalent inductance L_g and the equivalent resistance r_{Lg}.

During operation, depending on the wind speed, V_g varies between 130V and 400V. The values of L_g and r_{Lg} components, which have an important influence on the system frequency behavior, were calculated from the PMSG parameters determined by experimental methods ($L_g = 30$mH; $r_{Lg} = 0.95\Omega$).

It was found through analytical investigation that SIHDC output capacitor, C_{out}, and its equivalent series resistance r_{Cout} have insignificant influence on stability, due to the very high value of the supercapacitor capacitance C_S. Moreover, the influence of the supercapacitor parasitic resistance can be neglected.

The following hypotheses are considered valid for stability analysis:

(a) The power switching devices S_1, D_1 and D_2 are ideal;
(b) V_g and V_{out} (V_{Cs}) have constant values during one switching period T;
(c) L_1 and L_2 have equal inductance values, and the series resistances r_{L1} and r_{L2} are also equal;
(d) C_{in} has an equivalent series resistance r_{Cin}.

There are three state variables, defined in the following way:

- x_1 - the current through L_g, which is also the converter input current, I_{in};
- x_2 - the voltage across C_{in};
- x_3 - the current through L_1; x_3 is also equal to L_2 current because $L_1 = L_2$.

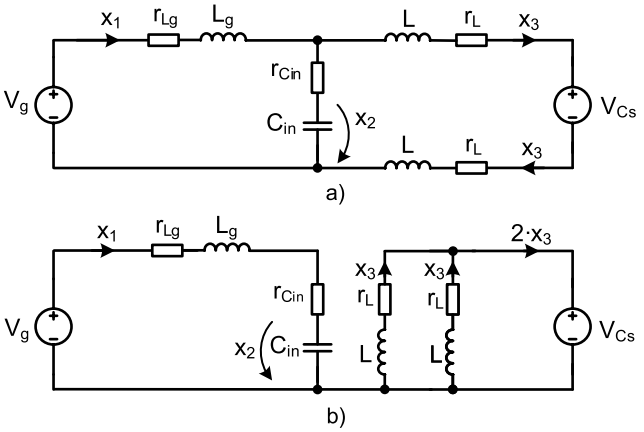

FIGURE 9. Equivalent circuits, derived from Fig. 8, used to obtain the equivalent average model through SSA method: a) for t_{on}; b) for t_{off}.

Fig. 9 presents the equivalent system circuits derived from Fig. 8, for the two S_1 states. The first circuit is valid for $t_{on} = D \cdot T$, the second one for $t_{off} = (1 - D) \cdot T$.

The state and output equations for t_{on} and the matrices representing the equation system are given in (15)-(17). The following notations are used: $L = L_1 = L_2$ and $r_L = r_{L1} = r_{L2}$. The control variable, which is also the output of the state-space model (y), is the S_1 switch current. In t_{on} time interval, the current through S_1 switch is equal to the inductor L_1 current.

$$\dot{x} = A_1 \cdot x + B_1 \cdot u, \quad x = \begin{bmatrix} x_1 \\ x_2 \\ x_3 \end{bmatrix} = \begin{bmatrix} i_{L_g} \\ v_{Cin} \\ i_L \end{bmatrix}, \quad u = \begin{bmatrix} V_g \\ V_{Cs} \end{bmatrix} \tag{15}$$

$$A_1 = \begin{bmatrix} -\frac{r_{L_g}+r_{C_{in}}}{L_g} & -\frac{1}{L_g} & \frac{r_{C_{in}}}{L_g} \\ \frac{1}{C_{in}} & 0 & -\frac{1}{C_{in}} \\ \frac{r_{C_{in}}}{2L} & \frac{1}{2L} & -\frac{r_{C_{in}}+2r_L}{2L} \end{bmatrix},$$

$$B_1 = \begin{bmatrix} \frac{1}{L_g} & 0 \\ 0 & 0 \\ 0 & -\frac{1}{2L} \end{bmatrix} \quad (16)$$

$$y = x_3 = C_1 \cdot x, \quad C_1 = \begin{bmatrix} 0 & 0 & 1 \end{bmatrix} \quad (17)$$

During t_{off}, the transistor current is zero. The state-space equations are:

$$\dot{x} = A_2 \cdot x + B_2 \cdot u, \quad (18)$$

$$A_2 = \begin{bmatrix} -\frac{r_{L_g}+r_{C_{in}}}{L_g} & -\frac{1}{L_g} & 0 \\ \frac{1}{C_{in}} & 0 & 0 \\ 0 & 0 & -\frac{r_L}{L} \end{bmatrix},$$

$$B_2 = \begin{bmatrix} \frac{1}{L_g} & 0 \\ 0 & 0 \\ 0 & -\frac{1}{L} \end{bmatrix}, \quad (19)$$

$$y = 0 = C_2 \cdot x, \quad C_2 = \begin{bmatrix} 0 & 0 & 0 \end{bmatrix}. \quad (20)$$

According to SSA method, the continuous-time, equivalent average model of the system is given by:

$$\begin{cases} \dot{x} = A \cdot x + B \cdot u \\ y = C \cdot x \end{cases}, \quad (21)$$

where matrices A, B and C are obtained from A_i, B_i and C_i, $i = 1, 2$, through a weighted summation:

$$A = A_1 \cdot D + A_2 \cdot (1 - D), \quad (22)$$

$$A = \begin{bmatrix} -\frac{r_{L_g}+r_{C_{in}}}{L_g} & -\frac{1}{L_g} & \frac{r_{C_{in}}}{L_g} \cdot D \\ \frac{1}{C_{in}} & 0 & -\frac{1}{C_{in}} \cdot D \\ \frac{r_{C_{in}}}{2L} \cdot D & \frac{D}{2L} & -\frac{2r_L + r_{C_{in}} \cdot D}{2L} \end{bmatrix}, \quad (23)$$

$$B = B_1 \cdot D + B_2 \cdot (1 - D) = \begin{bmatrix} \frac{1}{L_g} & 0 \\ 0 & 0 \\ 0 & -\frac{2-D}{2L} \end{bmatrix}, \quad (24)$$

$$C = C_1 \cdot D + C_2 \cdot (1 - D) = \begin{bmatrix} 0 & 0 & D \end{bmatrix}. \quad (25)$$

For the state-space equation system (21)-(25) of the equivalent average model, the small-signal transfer function of the output variable y [27] is:

$$\frac{\tilde{y}(s)}{\tilde{d}(s)} = \frac{\tilde{i}_{S_1}}{\tilde{d}(s)} = C \cdot [s \cdot I - A]^{-1} \cdot [(A_1 - A_2) \cdot X_0 + (B_1 - B_2).u] + (C_1 - C_2) \cdot X_0 \quad (26)$$

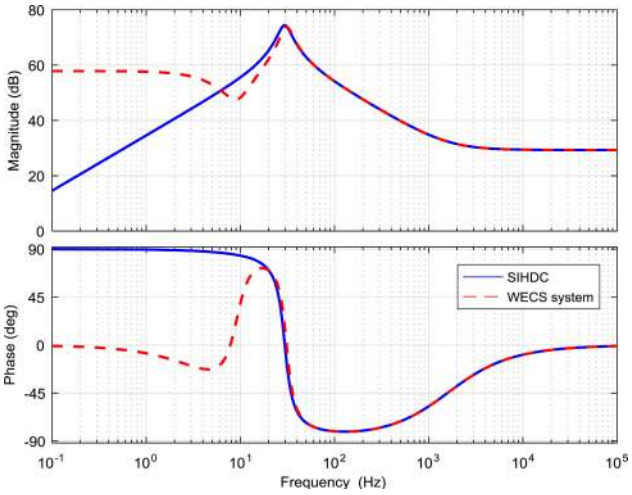

FIGURE 10. Bode diagrams of $\tilde{i}_{S_1}(s)/\tilde{d}(s)$ small-signal transfer function for SIHDC supplied: by a DC voltage source, and by PMSG in WECS. CCM operating point: $I_{Lg} = 10$A; $V_g = 300$V; $V_{Cs} = 60$V.

where

$$X_0 = -\left(A^{-1} \cdot B\right) \cdot u \quad (27)$$

represents the steady-state operating point for which the stability is evaluated, and $\tilde{i}_{S1}$ and $\tilde{d}$ are the small variations of i_{S1} and d.

Equation (26) can be written as:

$$G_P(s) = \frac{\tilde{y}(s)}{\tilde{d}(s)} = \frac{\tilde{i}_{S1}(s)}{\tilde{d}(s)} = \frac{a_3 s^3 + a_2 s^2 + a_1 s + a_0}{b_3 s^3 + b_2 s^2 + b_1 s + b_0} \quad (28)$$

The coefficients from (28) were obtained based on the terms of the calculation results given by a symbolic mathematics package. Afterwards, these terms were grouped and simplified. Coefficients a_0 to a_3 and b_0 to b_3, whose expressions are given in Appendix, are functions of the duty cycle D (that is present at different powers) and all the elements from Fig. 9: component values - including those of the PMSG DC equivalent model -, parasitic elements and the input and output voltages.

Equation (28), together with the equations of the coefficients, form a parameterized small-signal transfer function of the controlled variable (i_{S1}) that can be used for any similar WECS, to quickly obtain the particularized transfer function, base on which the stability of the system is evaluated.

To highlight the influence of the PMSG DC equivalent model on $\tilde{i}_{S_1}(s)/\tilde{d}(s)$ small-signal transfer function, its Bode diagram is represented in Fig. 10 in two situations, for the same operating point ($I_{Lg} = 10$A; $V_g = 300$V; $V_{Cs} = 60$V).

If the converter is supplied by a DC voltage source, the Bode diagram is the one plotted with continuous line. Actually, this represents the own SIHDC transfer function when the control variable is the average value of the transistor current. The *converter equivalent average model* is obtained from the system model described above, by removing: the first row and the first column from A_1 and A_2 matrixes,

the first row from B_1 and B_2 matrixes, and the first element from C_1 and C_2 vectors.

If SIHDC is supplied by PMSG as in Fig. 1 and Fig. 8, the Bode diagram follows the dashed line. Important differences between the two diagrams can be noted in low frequency range, as is expected due to the L_g impact. Comparable dissimilarities were noticed for other operating points in CCM.

The Bode diagrams of the WECS small-signal transfer function $\tilde{i}_{S_1}(s)/\tilde{d}(s)(\tilde{y}(s)/\tilde{d}(s))$ for three operating points ($I_{\mathrm{Lg}} = 10\mathrm{A}$; $V_{\mathrm{g}} = 130, 250, 400\mathrm{V}$; $V_{\mathrm{Cs}} = 60\mathrm{V}$) are presented in Fig. 11.

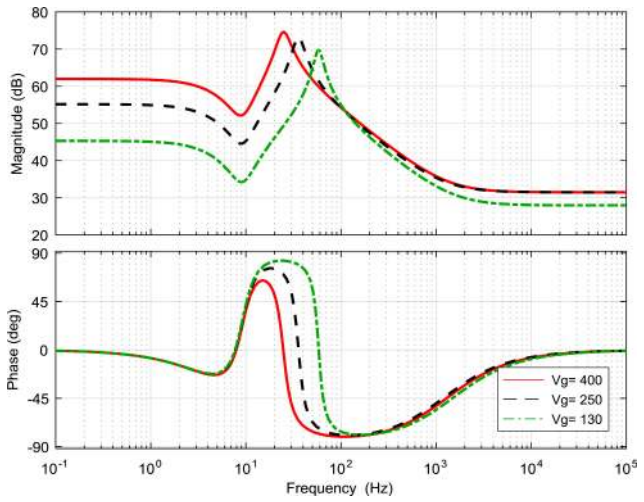

FIGURE 11. Bode diagrams of $\tilde{i}_{S_1}(s)/\tilde{d}(s)$ small-signal transfer function for SIHDC supplied: by a DC voltage source, and by PMSG in WECS. CCM operating point: $I_{Lg} = 10\mathrm{A}$; $V_g = 130, 250, 400\mathrm{V}$; $V_{Cs} = 60\mathrm{V}$.

The magnitude is influenced by V_{g} at low frequencies, and the phase curve is affected by V_{g} variations in the frequency range $[10^1, 10^2]$ Hz. Contrarily, in $[10^2, 10^3]$ Hz interval, the magnitude and phase are almost insensitive to V_{g} change. This behavior was also noted for the other two variables which determine the steady-state operating point, I_{Lg} and V_{Cs}. Consequently, if the SIHDC controller is designed for a cutoff frequency between 10^2Hz and 10^3Hz, the stability is not compromised by the change of the operating point.

B. PWM SWITCH MODEL (PWMSM) METHOD

This method was proposed in the literature as a way to obtain the equivalent average model of a power converter using a general-purpose electronic circuit simulation software like SPICE.

The non-linearity is treated exactly where it appears in the circuit, not globally as in the case of SSA method. The number of power transistors in the circuit must be equal to that of diodes, because a PWM Switch model is an equivalent average model for a transistor/diode pair.

Therefore, in order to use PWMSM for SIHDC, a transistor should be introduced in the circuit, with the constraint that nothing will be changed in the converter operation, waveforms and theory. The appropriate position for this insertion is in the bottom part of the schematic. The new circuit is presented in Fig. 12, already prepared for application of the PWMSM method. S_1 and S_2 power switches are driven synchronously to guarantee the equivalence with the original schematic.

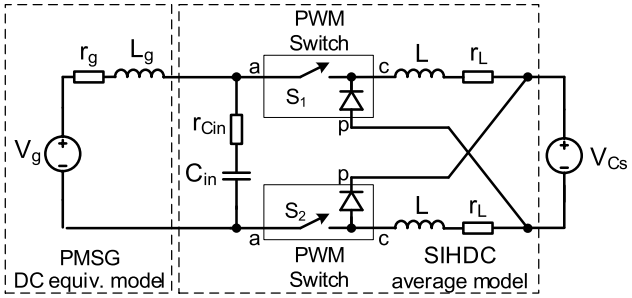

FIGURE 12. Equivalent average model based on the PWM switch model.

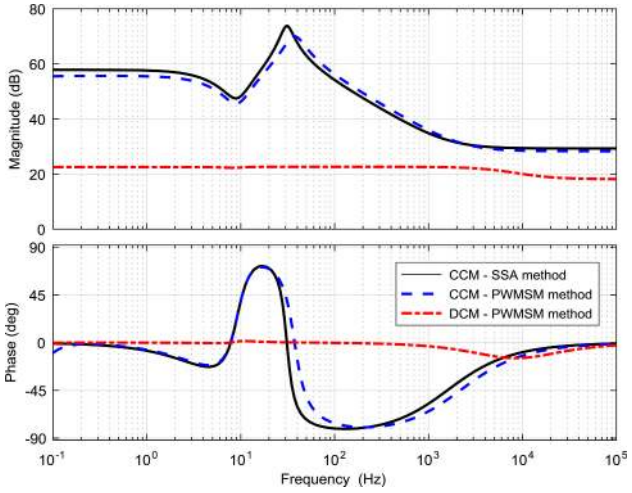

FIGURE 13. Bode diagrams of the WECS small-signal transfer function $\tilde{i}_{S_1}(s)/\tilde{d}(s)$, for CCM ($I_{Lg} = 10\mathrm{A}$, $V_g = 300\mathrm{V}$, $V_{Cs} = 60\mathrm{V}$) and DCM ($I_{Lg} = 2\mathrm{A}$, $V_g = 300\mathrm{V}$, $V_{Cs} = 60\mathrm{V}$), obtained through SSA and PWMSM methods.

Fig. 13 shows the Bode diagram of the WECS small-signal transfer function $\tilde{i}_{S_1}(s)/\tilde{d}(s)$ obtained in SPICE using the model from Fig. 12. The special procedure used for this purpose is presented in [28]. The SSA Bode diagram for the same operating point in CCM is also given, in order to compare the two results. As can be seen, there is a small difference between the plots, which means that the SPICE model based on PWMSM can be used with confidence.

One advantage of the PWMSM method implemented in SPICE is that the same simulation model can be used for CCM or DCM. Moreover, smooth transition between CCM and DCM can be assured in transient simulations [28]. The third Bode diagram shown in Fig. 13 was obtained for a DCM operating point ($I_{\mathrm{Lg}} = 2\mathrm{A}$; $V_{\mathrm{g}} = 300\mathrm{V}$; $V_{\mathrm{Cs}} = 60\mathrm{V}$).

For DCM operation, as opposed to CCM operation, the Bode diagrams of SIHDC and WECS small-signal transfer functions show irrelevant differences at all frequencies, as Fig. 14 shows.

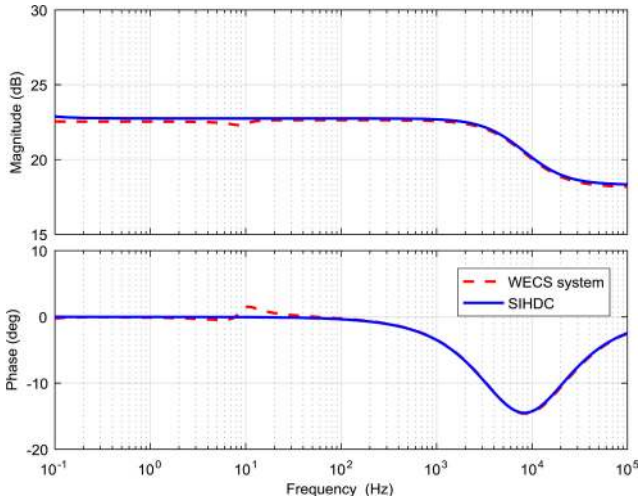

FIGURE 14. Bode diagrams of $\tilde{i}_{S_1}(s)/\tilde{d}(s)$ small-signal transfer function for SIHDC supplied: by a DC voltage source, and by PMSG in WECS. DCM operating point: $I_{Lg} = 2A$, $V_g = 300V$, $V_{Cs} = 60V$.

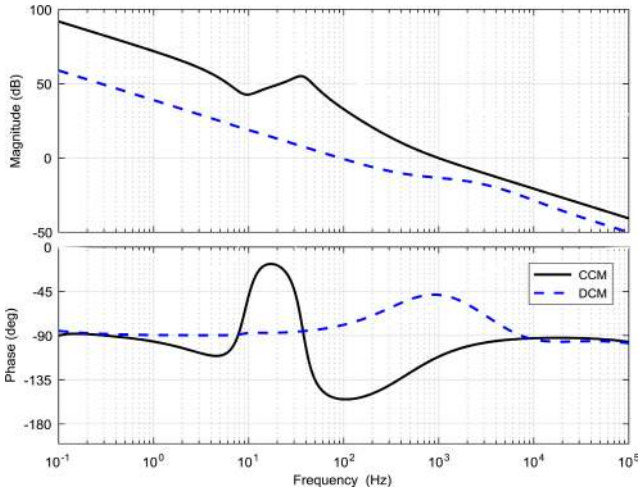

FIGURE 15. Bode diagrams of the open-loop small-signal transfer function for the system with controller, for two operating points: $I_{Lg} = 10A$, $V_g = 300V$, $V_{Cs} = 60V$ (CCM) and $I_{Lg} = 2A$, $V_g = 300V$, $V_{Cs} = 60V$ (DCM).

Combining the information obtained through SSA and PWMSM methods, the current controller can be designed and subsequently the WECS stability can be verified for any operating condition, CCM or DCM.

C. CONTROLLER DESIGN

The current controller was designed according to the K factor method [29] , starting from the Bode plots of the control variable in CCM, presented in Fig. 11 and Fig. 13. The stability was then checked for DCM.

The following controller transfer function provides a phase margin of PM = 70° at the cutting frequency $f_c = 1$kHz:

$$G_c(s) = k_c \cdot \frac{1 + \frac{s}{\omega_z}}{s \cdot \left(1 + \frac{s}{\omega_p}\right)}, \tag{29}$$

where:

$$k_c = 1540; \quad \omega_z = 2610 \text{ rad/s}; \\ \omega_p = 15150 \text{ rad/s}. \tag{30}$$

With G_c(s) expressed by (29) and (30) introduced in the system, the Bode diagrams of the overall open-loop small-signal transfer function for two operating points, in CCM and DCM respectively, look as in Fig. 15.

In CCM the phase margin of 70° for $f_c = 1$kHz is confirmed. What is interesting to note in DCM is the shifting of f_c from 1kHz to 100Hz, which together with a phase margin of 100° means a much slower response in i_{S1} average current settling than for CCM (not a problem for WECS application, due to the slow time constant of the mechanical subsystem). The stability is preserved in DCM, which is absolutely necessary.

V. SIHDC EFFICIENCY

The losses in power switching devices were calculated employing the measured data provided in transistor and diode datasheets (static characteristics, turn-on and turn-off energies, temperature influence, etc.). The types of power switching devices used for SIHDC prototype construction and the external gate resistance, R_G, which has influence on S_1 switching losses, are listed in Table 3, Section VI.

The conduction losses in transistor, averaged for one switching period, were calculated using the following equation:

$$\begin{aligned} P_{cond,S_1} &= \frac{1}{T} \cdot \int_{t_{on}} v_{CE}(t) \cdot i_{S_1}(t) \cdot dt \\ &= \frac{1}{T} \cdot \int_{t_{on}} V_{CE0} \cdot i_{S_1}(t) \cdot dt + \frac{1}{T} \cdot \int_{t_{on}} r_{CE} \cdot i_{S_1}^2(t) \cdot dt \\ &= V_{CE0} \cdot I_{S_1,avg} + r_{CE} \cdot I_{S_1,RMS}^2. \end{aligned} \tag{31}$$

In (31), the voltage across S_1 during conduction was modeled using the standard approach: the collector-emitter threshold voltage, V_{CE0}, in series with the dynamic resistance, r_{CE}. V_{CE0} and r_{CE} were extracted from the transistor static characteristic curve presented in the datasheet. The average and RMS values were calculated for each operating point used in efficiency evaluation, starting from S_1 current waveform.

Transistor switching losses, averaged for one switching period, were obtained through the equation:

$$P_{sw,S_1} = \left(E_{on,S_1} + E_{off,S_1}\right) \cdot f_s. \tag{32}$$

The turn-on and turn-off energies, E_{on,S_1} and E_{off,S_1}, for each operating point, were estimated by scaling the data given in datasheet. The peak of the collector current determined at transistor switch-on by the diode reverse recovery current was taken into account when calculating the switching losses.

P_{cond,S_1} and P_{sw,S_1} were added together to obtain the total transistor losses.

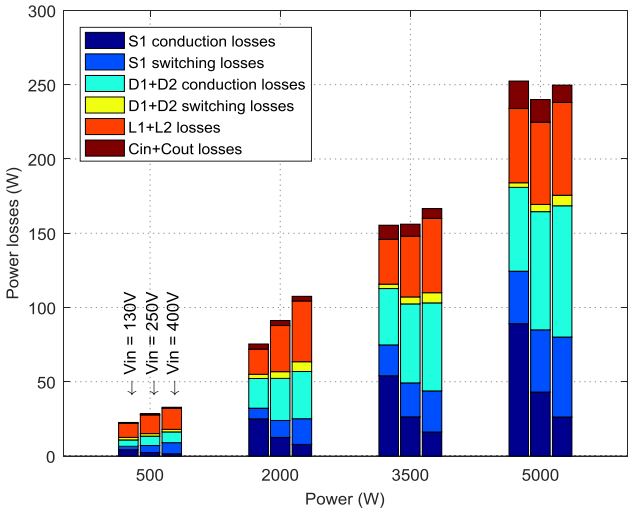

FIGURE 16. Distribution of power losses at four input power levels, for V_{in} = 130V, 250V, 400V.

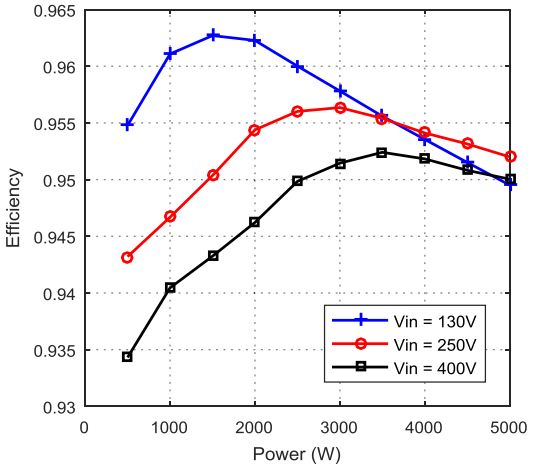

FIGURE 17. SIHDC efficiency as function of the input power, for V_{in} = 130V, 250V, 400V.

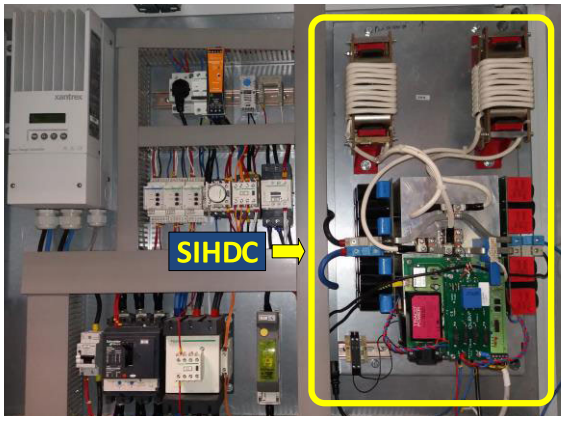

FIGURE 18. SIHDC prototype, mounted in an electrical enclosure together with electrical installation equipment, used for WECS testing in laboratory.

The conduction losses of one diode, averaged for one switching period, were computed by using the equation:

$$P_{cond,D_1} = V_{D0} \cdot I_{D_1,avg} + r_D \cdot I^2_{D_1,RMS}. \quad (33)$$

The threshold voltage, V_{D0}, and the dynamic resistance, r_D, were extracted from the diode static characteristic curve plotted in the datasheet.

The diode switching losses during the turn-on process were neglected, therefore only the turn-off energy was considered:

$$P_{sw,D_1} = E_{off,D_1} \cdot f_s. \quad (34)$$

The turn-off energy, E_{off,D_1}, was estimating for each operating point, by scaling the data from the datasheet.

The values obtained by (33) and (34) for one operating point were added to get the total power losses of one diode at that point.

The power losses in one inductor have two main components, P_{res,L_1} and P_{core,L_1}. The loss in the inductor series resistance was calculated by:

$$P_{res,L_1} = r_L \cdot I^2_{L_1,RMS}, \quad (35)$$

where r_L is the measured DC resistance of the inductor, given in Table 3, Section VI.

The specific core loss, expressed in W/kg for the alloy used to make the inductors, was calculated using the original Steinmetz equation:

$$P_{spec,core,L_1} = k \cdot f^{\alpha} \cdot \left(\frac{\Delta B}{2}\right)^{\beta}. \quad (36)$$

Although modified variants of this equation have been developed, that are affected by smaller errors at high or low duty cycle values, the original equation does not show significant errors for $0.2 < D < 0.8$ [30]. Only one operating point, out of the 30 where efficiency was calculated, had a duty cycle outside this range. Therefore, it can be considered that the specific core loss was correctly estimated.

In (36), the frequency is expressed in kHz. The AC component of B was calculated for each operating point. The values provided in the datasheet of the core material were used for the coefficients. They are:

$$k = 6.5; \quad \alpha = 1.51; \ \beta = 1.74. \quad (37)$$

The core losses, P_{core,L_1}, was evaluated by multiplying the specific core loss by the core mass, taken from the datasheet.

The power losses in the input and output capacitors, were obtained by using the equation:

$$P_C = R_{C,ESR} \cdot I^2_{C,RMS}. \quad (38)$$

The values of the equivalent series resistances are listed in Table 3, Section VI. The RMS current value was calculated based on the actual waveform, as with all other components.

Distribution of power losses at four input power levels, for V_{in} = 130V, 250V and 400V, is presented in Fig. 16.

TABLE 3. SIHDC prototype data.

Name	Meaning	Value
P_n	Rated power	5 kW
V_{in}	Input voltage range	120 - 400V
V_{out}	Output voltage range (in normal operation)	50 - 120V
L_1, L_2	Inductance of the switched inductor	170 µH
r_L	Inductor series resistance of L_1, L_2	6 mΩ
C_{in}	Input capacitance	10 mF
r_{Cin}	C_{in} equivalent series resistance	20 mΩ
C_{out}	Output capacitance	12 mF
r_{Cout}	C_{out} equivalent series resistance	20 mΩ
f_s	Switching frequency	9 kHz
R_G	Transistor external gate resistance	7.5 Ω
-	Transistor type (IGBT)	APT150GT120JR
-	Diode type	APT2X101DQ100J
-	Inductor core type	AMCC250
-	Inductor core material	2605SA1

TABLE 4. Wind turbine and PMSG data.

Name	Meaning	Value
	Wind Turbine	
N_p	Number of turbine blades	3
P_n	Rated power	5 kW
V_n	Rated wind speed	11 m/s
n_{max}	Maximum shaft speed	126 rpm
J_t	Total turbine inertia	140 kg·m^2
C_p	Maximum coefficient of power conversion	0.42
r_p	Radius of turbine blade	2.5 m
A_b	Blade swept area	19.6 m^2
	PMSG	
S_n	Rated power	5 kVA
p_p	Number of pole pares	16
N_c	Number of stator slots	33
f_n	Rated frequency	32 Hz
n_n	Rated shaft speed	120 rpm
V_g	Rectified voltage (DC equivalent model)	120 - 400 V
L_g	Inductance (DC equivalent model)	30 mH
R_g	Resistance (DC equivalent model)	0.95 Ω

Fig. 17 presents the SIHDC efficiency curves for $V_{in} = 130$V, 250V and 400V.

The input power was chosen as a reference for efficiency evaluation, because the converter controls the input current (and implicitly the power). Therefore, the efficiency was calculated by:

$$\eta = \frac{P_{in} - P_{loss,tot}}{P_{in}}. \tag{39}$$

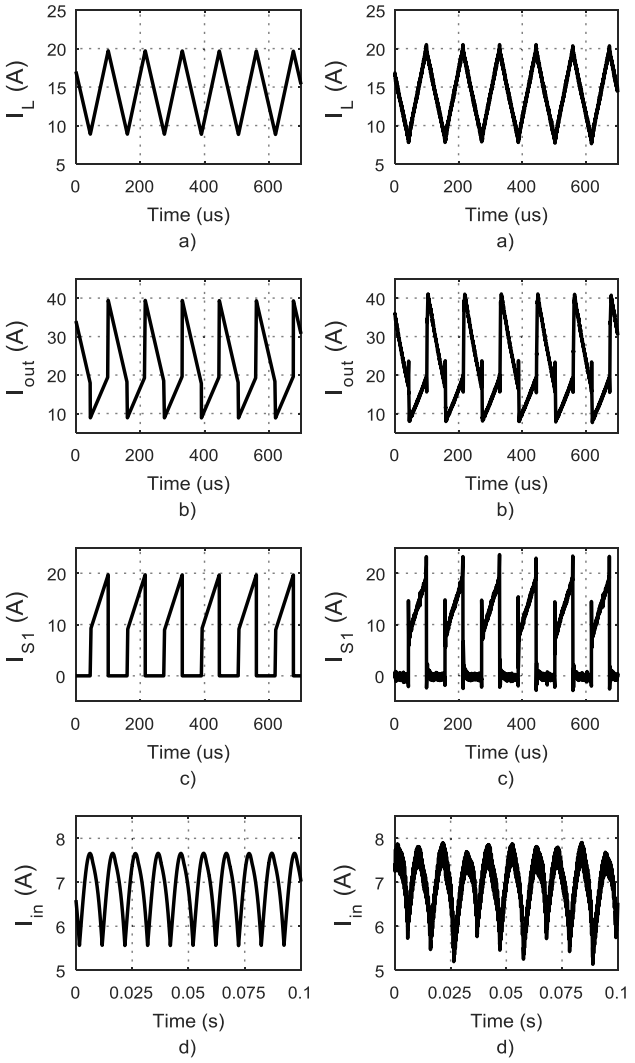

FIGURE 19. Key waveforms for steady-state CCM operation (I_{in} = 7A, V_{in} = 190V, V_{out} = 60V). Left: simulation data; right: experimental data acquired in laboratory. a) Inductor current; b) output current before the output capacitor; c) transistor current; d) input current (PMSG rectified current).

Total power losses, $P_{loss,tot}$, were obtained by summing all the loss components described above.

Regarding the power losses distribution, one fact clearly observed in Fig. 16 is the increasing of the diode conduction losses and the decreasing of the transistor conduction losses with the input voltage increasing. One the other hand, both diode and transistor switching losses rise at higher input voltage.

The SIHDC efficiency has a peak value above 96%, it is over 95% for half of the power range and it is greater than 94% for $P_{in} > 1$kW, which makes this converter an advantageous choice for the WECS application.

VI. SIMULATION AND EXPERIMENTAL RESULTS

A. LABORATORY TESTS

A SIHDC prototype, shown in Fig. 18, was built based on the information presented in previous sections. The prototype

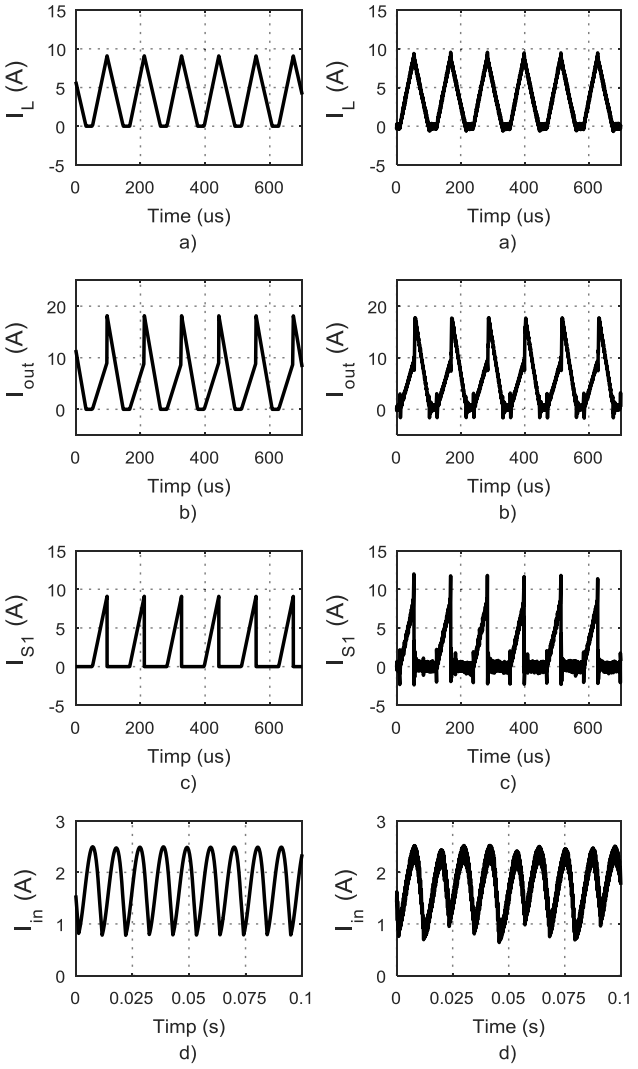

FIGURE 20. Key waveforms for steady-state DCM operation (I_{in} = 1.8A, V_{in} = 190V, V_{out} = 60V). Left: simulation data; right: experimental data acquired in laboratory. a) Inductor current; b) output current before the output capacitor; c) transistor current; d) input current (PMSG rectified current).

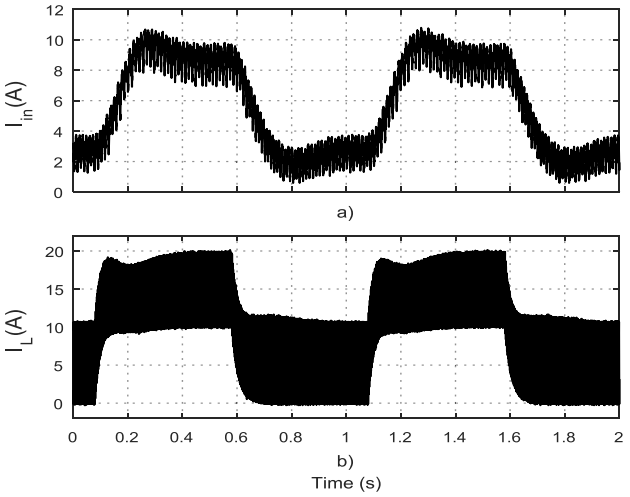

FIGURE 21. System response to a step change in iS1 average current reference. $I_{S1,ref}$ = 3 to 9A, V_{in} = 160V, V_{out} = 60V.

data are listed in Table 3. The main data of the wind turbine and PMSG included in the WECS are listed in VI-B. For laboratory testing, SIHDC input power is provided by a wind turbine emulator, comprised of an induction motor driven by a direct torque control frequency converter (for instantaneous control of speed and torque) and a PMSG identical with the generator used at the location where the real wind turbine was placed.

Fig. 19 presents the key waveforms, obtained both through simulation and through data acquisition from the prototype, in steady-state CCM operation, with $I_{\text{in}} = 7\text{A}$, $V_{\text{in}} = 190\text{V}$, $V_{\text{out}} = 60\text{V}$, at SIHDC input and output.

A good correspondence with the theoretical waveforms shown in Fig. 4 can be noticed for i_{L}, i_{S1} and i_{out}.

Input current i_{in} waveform, Fig. 19 d), is one specific for a three-phase rectified current. Although i_{in} frequency is much lower than the switching frequency, in steady-state operation its average value is equal to the mean value of the switch current i_{S1}. An important fact was noted, that even in the case of a light imbalance (10%-15%) of the PMSG phase inductances, which causes unequal phase currents as Fig. 19 shows, the average current value is kept constant.

The same waveforms are shown in Fig. 20 for steady-state DCM operation, with $I_{\text{in}} = 1.8\text{A}$, $V_{\text{in}} = 190\text{V}$, $V_{\text{out}} = 60\text{V}$. The comments on the CCM case are valid in this case as well.

The effect on i_{in}, of a step change in i_{S1} average current reference is exemplified in Fig. 21. The filter formed by PMSG phase inductances and C_{in} causes latency in i_{in} waveform. In 300 ms the input current is settled at the new value. Given the slow wind turbine dynamics, this value is acceptable for WECS application. The inductor current and i_{S1} ($i_{\text{S1}} = i_{\text{L}}$ during t_{on}) are changing much quickly, as expected.

B. TESTING IN REAL OPERATING CONDITIONS

Real conditions testing was done on a WECS identic with that tested in laboratory, but the generator was mechanically connected to a 5kW wind turbine, mounted at a top of a 15m tower. A picture of the place where the turbine and WECS are located is presented in Fig. 22. The wind turbine control system includes a fuzzy logic based MPPT algorithm similar to that presented in [29].

Fig. 23 gives a few selected WECS data, acquired through the local SCADA system. I_{in} current is controlled by SIHDC to keep the wind turbine in the maximum power point at each moment. An industrial programmable logic controller (PLC) was used to measure the relevant physical quantities, to calculate the I_{in} reference current, to coordinate the circuit protection devices and to connect additional loads if the supercapacitor voltage (V_{out}) is too high (Loads Control block from Fig. 1 is implemented in PLC).

A scenario for SC voltage control is illustrated in Fig. 24. A sustained high, or relatively high, input power in the case

FIGURE 22. Wind turbine photo. SIHDC is installed inside the metallic container located behind the tower.

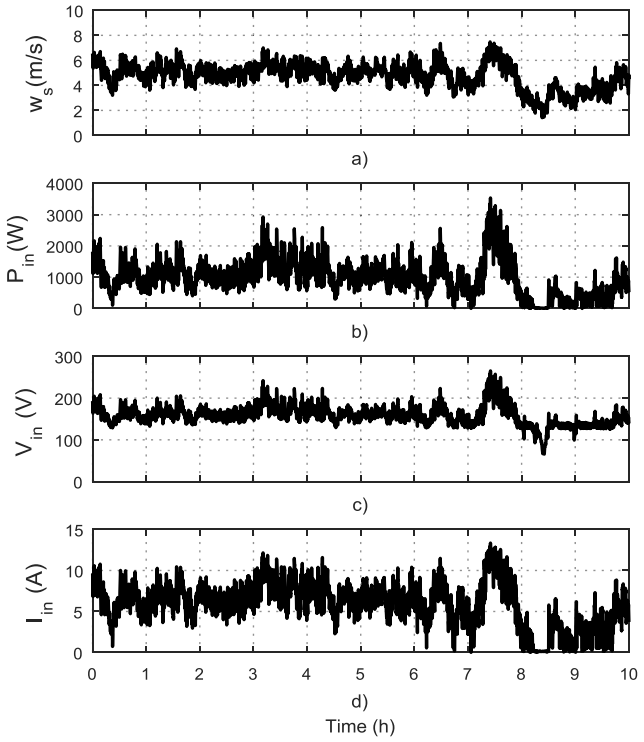

FIGURE 23. Experimental data obtained in real operating conditions. a) Wind speed; b) SIHDC input power; c) SIHDC input voltage; d) SIHDC input current.

of low total power consumption (loads and battery charging) leads to the increasing of the SC voltage up to 90V, which is one of the voltage control levels used in PLC. An additional load is connected at 90 V and the SC voltage decreases to 70 V, the control level used for load disconnection. After the additional load is disconnected, the SC voltage increases again to 90V, if the input power continues to be higher than the total consumed power. In this way, all the power provided by wind turbine can be converted and used to feed dc and ac loads. When the input power does not exceed the

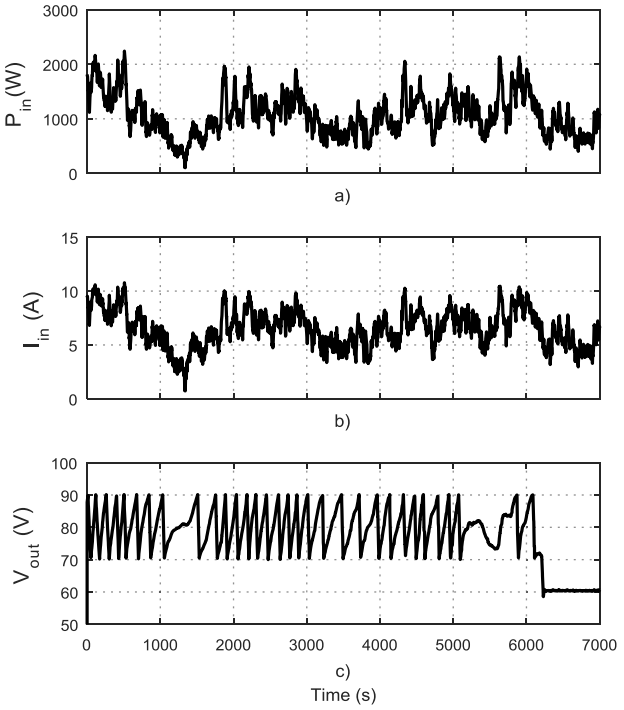

FIGURE 24. A scenario for SC voltage control. Experimental data obtained in real operating conditions. a) SIHDC input power; b) SIHDC input current; c) SIHDC output voltage (SC voltage).

consumption demand, the output voltage of SIHDC is maintained at 60V by the DC battery charger, directly connected to SC.

The WECS was monitored through the local SCADA system, and the theoretical analysis and laboratory tests results were confirmed.

VII. CONCLUSION

In a small power WECS with hybrid energy storage, the integrated step-down SIHDC is suitable for controlling the output power of the electric generator through converter average input current, in order to maintain the operation at the maximum power point.

The steady-state analysis for CCM and DCM specific for this application, reveals the relation between the converter average input current, the transistor and inductor currents, used for transistor selection and inductor design. For steady-state operation in CCM, the converter is running at a duty cycle which is up to two times higher than that of the classical buck converter operating with the same voltage conversion ratio. For steady-state operation in DCM the duty cycle can be calculated by a simple formula, if the required average value of the input current is given.

Stability analysis is presented in detail. The influence of the three-phase PMSG on the stability, very important in WECS application, is taken into consideration through a DC equivalent model. SSA method is used to obtain the continuous-time, equivalent average model, of the system for CCM. The parameterized analytical expression of the small-signal

transfer function of the control variable described in this paper can be quickly particularized for any similar WECS, and then used for system stability assessment. The results obtained through SSA were checked against the results given by the stability analysis method based on PWM Switch Model, which can be used in both continuous and discontinuous operating modes.

SIHDC current controller was designed for stable operation in CCM and afterwards the stability was checked in DCM, using small-signal transfer function Bode diagrams of the equivalent average models. A shifting down of the cutting frequency was noted in DCM, resulting in a slower response at light wind turbine power. The stability of the system was preserved in DCM, with better phase margin than in CCM.

A 5kW SIHDC prototype was built and then tested in laboratory and in the field. Laboratory tests, performed on a WECS powered by a wind turbine emulator, proved that SIHDC is able to control the PMSG output power and the operation is stable in both CCM and DCM. Experimental data obtained in real operating conditions from a 5kW wind turbine WECS monitored over an extended time period confirmed the theoretical analysis and the laboratory tests.

APPENDIX

The numerator and denominator coefficients of the small-signal transfer function from (28) are:

$$
\begin{aligned}
a_0 &= (r_{Cin} - r_{Lg})^2 \cdot D^4 - 2r_{Cin} \cdot (r_{Cin} - r_{Lg}) \cdot D^3 \\
&\quad + (r_{Cin}^2 - 4 \cdot r_L \cdot (r_{Cin} - r_{Lg})) \cdot D^2 \\
&\quad + 4 \cdot r_{Cin} \cdot r_L \cdot D + 4 \cdot r_L^2 \\
a_1 &= -(L_g - C_{in} \cdot r_{Cin}^2) \cdot (r_{Cin} - r_{Lg}) \cdot D^4 \\
&\quad - (C_{in} \cdot r_{Cin} \cdot (r_{Cin} + r_{Lg}) \cdot (r_{Cin} - r_{Lg}) - r_{Cin} \\
&\quad \cdot (L_g - C_{in} \cdot r_{Cin}^2)) \cdot D^3 \\
&\quad + (C_{in} \cdot r_{Cin}^2 \cdot (r_{Cin} + r_{Lg}) - 2 \cdot (r_{Cin} - r_{Lg}) \\
&\quad \cdot (L + C_{in} \cdot r_L \cdot (r_{Cin} + r_{Lg}))) \cdot D^2 \\
&\quad + 2 \cdot r_L \cdot (L_g - C_{in} \cdot r_{Cin}^2) \cdot D^2 \\
&\quad + (2 \cdot C_{in} \cdot r_{Cin} \cdot r_L \cdot (r_{Cin} + r_{Lg}) + 2 \cdot r_{Cin} \\
&\quad \cdot (L + C_{in} \cdot r_L \cdot (r_{Cin} + r_{Lg}))) \cdot D \\
&\quad + 4 \cdot r_L \cdot (L + C_{in} \cdot r_L \cdot (r_{Cin} + r_{Lg})) \\
a_2 &= -C_{in} \cdot L_g \cdot r_{Cin} \cdot (r_{Cin} - r_{Lg}) \cdot D^3 \\
&\quad + C_{in} \cdot (L_g \cdot r_{Cin}^2 - 2 \cdot (r_{Cin} - r_{Lg}) \\
&\quad \cdot (L \cdot (r_{Cin} + r_{Lg}) + L_g \cdot r_L)) \cdot D^2 \\
&\quad + 2 \cdot C_{in} \cdot r_{Cin} \\
&\quad \cdot ((L \cdot (r_{Cin} + r_{Lg}) + L_g \cdot r_L) + L_g \cdot r_L) \cdot D \\
&\quad + 4 \cdot C_{in} \cdot r_L \cdot (L \cdot (r_{Cin} + r_{Lg}) + L_g \cdot r_L) \\
a_3 &= 2 \cdot C_{in} \cdot L \cdot L_g \cdot ((r_{Lg} - r_{Cin}) \cdot D^2 + r_{Cin} \cdot D + 2 \cdot r_L) \\
b_0 &= (r_{Cin} \cdot (V_g - V_{Cs}) + 2 \cdot r_{Lg} \cdot V_{Cs}) \cdot D^2 \\
&\quad + 4 \cdot r_L \cdot (V_g + V_{Cs}) \cdot D - 4 \cdot r_L \cdot V_{Cs} \\
b_1 &= C_{in} \cdot (r_{Cin}^2 \cdot (V_g - V_{Cs}) + 2 \cdot V_{Cs} \cdot r_{Lg}^2 + r_{Cin} \cdot r_{Lg} \\
&\quad \cdot (V_g + V_{Cs})) \cdot D^2 \\
&\quad + 2 \cdot (2 \cdot C_{in} \cdot r_{Cin} \cdot r_L + 2 \cdot C_{in} \cdot r_L \cdot r_{Lg} + L) \\
&\quad \cdot (V_g + V_{Cs}) \cdot D \\
&\quad - 4 \cdot (C_{in} \cdot r_L (r_{Cin} + r_{Lg}) + L) \cdot V_{Cs} \\
b_2 &= C_{in} \cdot L_g \cdot (r_{Cin} \\
&\quad \cdot (V_g - V_{Cs}) + 2 \cdot r_{Lg} \cdot V_{Cs}) \cdot D^2 \\
&\quad + 2 \cdot C_{in} \cdot (L \cdot r_{Cin} + L \cdot r_{Lg} + 2 \cdot L_g \cdot r_L) \\
&\quad \cdot (V_g + V_{Cs}) \cdot D \\
&\quad - 4 \cdot C_{in} \cdot (L \cdot (r_{Cin} + r_{Lg}) + L_g \cdot r_L) \cdot V_{Cs} \\
b_3 &= 2 \cdot C_{in} \cdot L \cdot L_g \cdot ((V_g + V_{Cs}) \cdot D - 2 \cdot V_{Cs})
\end{aligned}
$$

REFERENCES

[1] Z. Zhang, Z. Li, M. P. Kazmierkowski, J. Rodríguez, and R. Kennel, "Robust predictive control of three-level NPC back-to-back power converter PMSG wind turbine systems with revised predictions," *IEEE Trans. Power Electron.*, vol. 33, no. 11, pp. 9588–9598, Nov. 2018.

[2] P. Kou, D. Liang, L. Yu, and L. Gao, "Nonlinear model predictive control of wind farm for system frequency support," *IEEE Trans. Power Syst.*, vol. 34, no. 5, pp. 3547–3561, Sep. 2019.

[3] M. A. S. Ali, K. K. Mehmood, S. Baloch, and C.-H. Kim, "Wind-speed estimation and sensorless control for SPMSG-based WECS using LMI-based SMC," *IEEE Access*, vol. 8, pp. 26524–26535, 2020.

[4] J. Chen, T. Lin, C. Wen, and Y. Song, "Design of a unified power controller for variable-speed fixed-pitch wind energy conversion system," *IEEE Trans. Ind. Electron.*, vol. 63, no. 8, pp. 4899–4908, Aug. 2016.

[5] M. Rossander, A. Goude, and S. Eriksson, "Mechanical torque ripple from a passive diode rectifier in a 12 kW vertical axis wind turbine," *IEEE Trans. Energy Convers.*, vol. 32, no. 1, pp. 164–171, Mar. 2017.

[6] J. Chen and J. Chen, "On reducing the shaft torque ripple of small-to-medium-scale wind energy conversion systems using multi-pulse autotransformer rectifier," *Energies*, vol. 11, no. 2, p. 379, Feb. 2018.

[7] Y. Y. Xia, J. E. Fletcher, S. J. Finney, K. H. Ahmed, and B. W. Williams, "Torque ripple analysis and reduction for wind energy conversion systems using uncontrolled rectifier and boost converter," *IET Renew. Power Gener.*, vol. 5, no. 5, pp. 377–386, Sep. 2011.

[8] B. Axelrod, Y. Berkovich, and A. Ioinovici, "Switched-capacitor/switched-inductor structures for getting transformerless hybrid DC–DC PWM converters," *IEEE Trans. Circuits Syst. I, Reg. Papers*, vol. 55, no. 2, pp. 687–696, Mar. 2008.

[9] Y. Tang, D. Fu, T. Wang, and Z. Xu, "Hybrid switched-inductor converters for high step-up conversion," *IEEE Trans. Ind. Electron.*, vol. 62, no. 3, pp. 1480–1490, Mar. 2015.

[10] Y. Cao, V. Samavatian, K. Kaskani, and H. Eshraghi, "A novel nonisolated ultra-high-voltage-gain DC–DC converter with low voltage stress," *IEEE Trans. Ind. Electron.*, vol. 64, no. 4, pp. 2809–2819, Apr. 2017.

[11] J. Melo de Andrade, R. F. Coelho, and T. B. Lazzarin, "High step-up DC–DC converter based on modified active switched-inductor and switched-capacitor cells," *IET Power Electron.*, vol. 65, no. 7, pp. 5644–5654, Jul. 2018.

[12] M. Lakshmi and S. Hemamalini, "Nonisolated high gain DC–DC converter for DC microgrids," *IEEE Trans. Ind. Electron.*, vol. 65, no. 2, pp. 1205–1212, Feb. 2018.

[13] D. Hulea, B. Fahimi, N. Muntean, and O. Cornea, "High ratio bidirectional hybrid switched inductor converter using wide bandgap transistors," in *Proc. 20th Eur. Conf. Power Electron. Applic. (EPE ECCE Europe)*, Riga, Latvia, 2018, pp. P.1–P.10.

[14] K. Li, Y. Hu, and A. Ioinovici, "Generation of the large DC gain step-up nonisolated converters in conjunction with renewable energy sources starting from a proposed geometric structure," *IEEE Trans. Power Electron.*, vol. 32, no. 7, pp. 5323–5340, Jul. 2017.

[15] N. Muntean, O. Cornea, and D. Petrila, "A new conversion and control system for a small off–grid wind turbine," in *Proc. 12th Int. Conf. Optim. Electr. Electron. Equip. (OPTIM)*, Basov, Romania, May 2010, pp. 1167–1173.

[16] A. Berrueta, A. Ursúa, I. S. Martín, A. Eftekhari, and P. Sanchis, "Supercapacitors: Electrical characteristics, modeling, applications, and future trends," *IEEE Access*, vol. 7, pp. 50869–50896, 2019.

[17] M. Farhadi and O. Mohammed, "Energy storage technologies for high-power applications," *IEEE Trans. Ind. Appl.*, vol. 52, no. 3, pp. 1953–1961, Jun. 2016.
[18] N. A. Elessawy, J. El Nady, W. Wazeer, and A. B. Kashyout, "Development of high-performance supercapacitor based on a novel controllable green synthesis for 3D nitrogen doped graphene," *Sci. Rep.*, vol. 9, no. 1, pp. 1–10, Feb. 2019.
[19] H. Yang, S. Kannappan, A. S. Pandian, J.-H. Jang, Y. S. Lee, and W. Lu, "Graphene supercapacitor with both high power and energy density," *Nanotechnology*, vol. 28, no. 44, Oct. 2017, Art. no. 445401.
[20] F. Ortenzi, M. Pasquali, P. P. Prosini, A. Lidozzi, and M. Di Benedetto, "Design and validation of ultra-fast charging infrastructures based on supercapacitors for urban public transportation applications," *Energies*, vol. 12, no. 12, p. 2348, Jun. 2019.
[21] F. Castelli Dezza, V. Musolino, L. Piegari, and R. Rizzo, "Hybrid battery–supercapacitor system for full electric forklifts," *IET Electr. Syst. Transp.*, vol. 9, no. 1, pp. 16–23, Mar. 2019.
[22] O. Pelan, N. Muntean, O. Cornea, and F. Blaabjerg, "High voltage conversion ratio, switched C & L cells, step-down DC-DC converter," in *Proc. IEEE Energy Convers. Congr. Expo. (ECCE)*, Denver, CO, USA, Sep. 2013, pp. 5580–5585.
[23] M. Dalla Vecchia, G. Van den Broeck, S. Ravyts, and J. Driesen, "Novel step-down DC–DC converters based on the inductor–diode and inductor–capacitor–diode structures in a two-stage buck converter," *Energies*, vol. 12, no. 6, p. 1131, Mar. 2019.
[24] S. Misal and M. Veerachary, "Analysis of a fourth-order step-down converter," *IEEE Trans. Ind. Appl.*, vol. 56, no. 3, pp. 2773–2787, May/Jun. 2020.
[25] B. Zhu, S. Hu, G. Liu, Y. Huang, and X. She, "Low-voltage stress buck-boost converter with a high-voltage conversion gain," *IEEE Access*, vol. 8, pp. 95188–95196, 2020.
[26] D. Petrila, F. Blaabjerg, N. Muntean, and C. Lascu, "Fuzzy logic based MPPT controller for a small wind turbine system," in *Proc. 13th Int. Conf. Optim. Electr. Electron. Equip. (OPTIM)*, Brasov, Romania, May 2012, pp. 993–999.
[27] A. Ioinovici, *Power Electronics and Energy Conversion Systems, Fundamentals and Hard-switching Converters*, vol. 1. Chichester, U.K.: Wiley, 2013, chs. 2.2–2.5, pp. 164–288.
[28] C. P. Basso, *Switch Mode Power Supplies. SPICE Simulations and Practical Design*. New York, NY, USA: McGraw-Hill, 2008, pp. 111–145 and 241–285.
[29] V. Vorperian, "Simplified analysis of PWM converters using model of PWM switch. Continuous conduction mode," *IEEE Trans. Aerosp. Electron. Syst.*, vol. 26, no. 3, pp. 490–496, May 1990.
[30] A. Van den Bossche, V. C. Valchev, and G. B. Georgiev, "Measurement and loss model of ferrites with non-sinusoidal waveforms," in *Proc. IEEE 35th Annu. Power Electron. Specialists Conf. Aachen, Germany*, vol. 2004, pp. 4814–4818.

OCTAVIAN CORNEA (Member, IEEE) received the B.S., M.S., and Ph.D. degrees in electrical engineering from Politehnica University Timisoara, Romania.

He is currently a Lecturer with Politehnica University Timisoara. He has been involved in several research projects in various fields, including renewable energy and microgrids. He has authored or coauthored more than 40 scientific articles in power electronics, renewable energy, and SRM drives. His main research interests include modeling, simulation, and control of power electronic converters in different kinds of applications.

DAN HULEA (Student Member, IEEE) received the B.Eng. and M.Eng. degrees in electrical engineering from Politehnica University Timisoara, Romania, in 2014 and 2016, respectively, where he is currently pursuing the Ph.D. degree.

Since 2014, he has been a Research Assistant at Politehnica University Timisoara. He was a Visiting Scientist with The University of Texas at Dallas, in 2017, for a period of five months. His research interests include bidirectional high-ratio dc–dc power converters and their application for storage systems in microgrid structures.

Mr. Hulea was a recipient of the IEEE IES Student Paper Travel Award, in 2015, and the EPE Young Author Best Paper Award, in 2019.

NICOLAE MUNTEAN (Senior Member, IEEE) received the B.Sc. and Ph.D. degrees from Politehnica University Timisoara, România.

He has authored over 70 publications in the field of power electronics, including four books (as a single author or coauthor). His research interest includes industrial implementation of power electronics systems in various applications. He is currently involved in research and development related to renewable energy systems.

Dr. Muntean is an Associate Editor of the *Journal of Electric Engineering*.

GHEORGHE-DANIEL ANDREESCU (Senior Member, IEEE) was born in Caracal, Romania. He received the M.S. degree in applied electronics and the Ph.D. degree in automatic control systems from Politehnica University Timisoara, Romania, in 1977 and 1999, respectively.

Since 1984, he has been with the Automation and Applied Informatics Department, Politehnica University Timisoara, where he is currently a Full Professor. He has authored or coauthored over 80 articles in international journals and conference proceedings. His main research interests include advanced control of ac drives, sensorless control, observers, sliding-mode control, power electronics control, mechatronic systems, and real-time implementations.

Dr. Andreescu is a member of the Technical Committee TC4.2 Mechatronics Systems of the International Federation of Automatic Control (IFAC) and has been a member of the Engineering Sciences Commission of the National University Research Council.